Cam Ring Curve Optimization for Radial Hydraulic Motor Based on Seagull Algorithm

Bowen Zhang – Shaopeng Kang✉ – Runze Zhou – Hongbin Qiang – Jing Yang – Kailei Liu – Yunkai Zhou
Jiangsu University of Technology, School of Mechanical Engineering, China
✉ ksp@jsut.edu.cn

Abstract *With the accelerated adjustment of the global energy structure, the intensity of strategic mineral resource development continues to rise. The growing demand for construction machinery and equipment has led to increased use of radial piston hydraulic motors, known for their low-speed and high-torque characteristics, in heavy-duty mining machinery and equipment. However, the cam ring curve design of a radial piston hydraulic motor still faces critical challenges, including significant contact stress, and noticeable output pulsation. To address these issues, this paper proposes a multi-step composite curve optimization design method based on the seagull optimization algorithm (SOA). This method integrates the concepts of stepped and trapezoidal acceleration curve design, utilizing the SOA algorithm to tackle these challenges. The SOA algorithm is more adaptive than the genetic algorithm and the particle swarm optimization algorithm, maintaining population diversity even in the later stages of iteration. This effectively overcomes the limitations of the particle swarm optimization and genetic algorithm in multi-peak problems. A cam ring curve optimization model is established to minimizing contact stress through theoretical modeling and dynamics analysis. Using the combined global search and local exploitation capabilities of SOA, we achieved multi-constraint optimization on key parameters such as the amplitude-angle ratio in the acceleration zone and the amplitude-angle in the zero-speed zone. This results in a composite cam ring curve characterized by reduced stress, low pulsation, and shock-free operation. The effectiveness of this method was validated through bench tests, which showed that the maximum contact stress of the optimized multistep composite curve at a speed of 100 rpm is reduced by 5.4 % and 18.3 % compared to the conventional equal acceleration curve and trapezoidal curve, respectively. Additionally, the speed pulsation rate decreases by 10.81 % and 25.73 % under 20 MPa and 30 MPa conditions, respectively, with no sudden change in reaction force and a reduction in pulsation shock during operation.*

Keywords *radial piston hydraulic motor, cam ring optimization, seagull optimization algorithm, contact stress, speed pulsation*

Highlights

- *Proposed a multi-step composite curve optimization design method based on the Seagull Optimization Algorithm.*
- *Demonstrated the effect of cam ring curve on motor performance.*
- *Revealed superior adaptability and population diversity preservation in multi-peak problems.*
- *Confirmed optimized smoothness and energy efficiency of hydraulic motors.*

1 INTRODUCTION

Radial piston hydraulic motors are the core driving elements of medium- and large-sized machinery and equipment. Due to their high stability at low speeds and excellent starting efficiency, they are widely used in construction machinery, ships, and other applications [1-3] . The cam ring is the key element of the in-curve radial piston hydraulic motor, as it governs the macroscopic motion behavior of the roller-plunger-cylinder assembly. Different theoretical design approaches can lead to different component motion patterns [4-5]. Assuming that the input hydraulic fluid oil pressure remains constant and the instantaneous output torque of the motor is the sum of the tangential component forces generated by each plunger pair on the rotary axis [6-7], synthetic torque pulsation can be reduced by optimizing the cam ring curve without considering external factors.

As the component consistently interacts with the cam ring during operation, it is susceptible to shock and vibration under high oil pressure and high-speed conditions. Optimizing the design method of the cam ring curve can effectively reduce both the output torque pulsation and speed pulsation of the motor. In the early stages, due to the limitation of processing technology and machining equipment, the cam rings were primarily designed using simple and easy-to-machine curves, such as arcs and straight lines [8]. However, the discontinuous curvature at the joints caused sudden changes in the acceleration of the piston, leading to periodical fluctuations in the output torque of the hydraulic motor and resulting in prominent pulsations. With the development of high-precision machining techniques and equipment, the design methods for curves have become diversified [9], contribution to reduced speed pulsation and torque pulsation in hydraulic motors [10-11]. Many scholars and engineers have proposed various solutions aimed at achieving smoother operation, longer service life, and lower pulsation rates. Giljen et al. [12] used the variable speed technology effectively optimizing the performance of water pumps under different operating conditions. The internal transient flow is extremely complex, causing unstable phenomena such as eddy currents and backflow. Research on these flow characteristics is of great significance for ensuring the safe and stable operation of the unit and improving efficiency. Tang et al. [13] used surface texturing technology to regulate the friction interface characteristics and explore the influence of groove texturing on vibration characteristics at different speeds. Gao et al. [14] established a life assessment model, the effectiveness of the life assessment method with crankshaft bearings as key components, providing a reference for contact stress analysis in this study. Chen et al. [15] designed a conical gear pair with a vertical tooth profile to improve its transmission performance in microfabrication and refine the design theory. Zhang et al. [16] proposed a genetic algorithm-based design method for optimizing the high-order cam ring curves, effectively reducing pulsation rate, and ensuring smooth, shock-free transitions between speed intervals. Li et al. [17] used an improved

DOI: 10.5545/sv-jme.2025.1394

particle swarm algorithm to optimize the partition amplitude angle to mitigate fatigue wear and reduce impact effectively. Zhou et al. [18] employed the Fourier series to describe the displacement function of the follower in a high-speed cam mechanism, which effectively reduced vibration and shock velocity. Chao et al. [19] proposed an optimal design method for pre-compensation of cam ring deformation, which couples the effect of elastic deformation during the design stage to reduce the motor pulsation thus enhancing the stability of the motor. Despite the progress made in reducing the pulsation in radial piston motors, further progress is needed to better optimize the impact and contact stresses.

Despite advancements in cam ring curve design, radial piston hydraulic motors continue to exhibit shocks, pulsations, and limited cam ring service life. The study proposes a multi-step composite curve design that combines the low-stress characteristics of the stepped curve with the shock-free advantages of the trapezoidal curve, introducing the seagull optimisation algorithm (SOA) optimization algorithm to achieve global parameter optimization and reduce shocks and pulsations during motor motion. First, a typical radial piston motor's motion, force, and deformation characteristics are analyzed in detail. Secondly, a multi-amplitude angular partition optimization method is established to optimize the cam ring curve, thereby reducing pulsation of the motor. Finally, the effectiveness of the multi-step composite curve optimization design method is verified through bench tests. This study combines SOA with cam ring design for the first time, providing a new practical strategy for reducing shock and improving operational stability in radial piston hydraulic motors, while contributing significantly to the broader optimization of fluid transmission systems.

2 METHODS & MATERIALS

Internal curve radial piston hydraulic motors can operate in multiple modes of action and be switched to various functions according to the load conditions and the application environment to meet the needs of diverse industries. The operating principle of the motor is shown in Fig. 1. During operation, the hydraulic pump extracts hydraulic oil from the tank and conveys it through the pipeline to the inlet port of the motor. The high-pressure hydraulic oil entering motor then flows into the piston chamber where the pressure acts on the bottom of the piston, pushing the piston outward. During the return stroke, the piston assembly presses the low-pressure fluid from the piston chamber to the return port. Due to the geometry of the inner curve combined with the piston-roller assembly, the assembly moves at a certain pressure angle, which ensure torque transmission and power output. Under the continuous action of hydraulic oil, the piston drives the roller to complete a lift-and-return motion along the cam ring rail. One complete lift and return constitutes an action interval, and the cam ring curve consists of several action intervals.

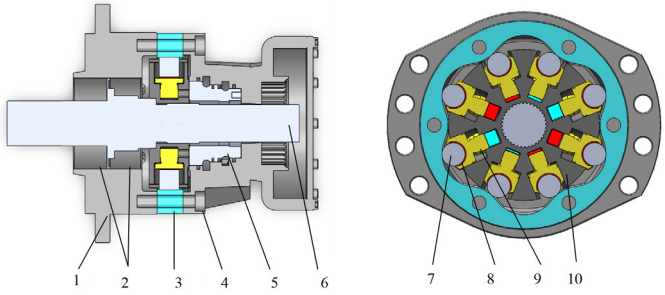

Fig. 1. Schematic diagram of motor structure;
1. front cover assembly, 2. bearing, 3. cam ring, 4. rear cover assembly, 5. distributor valve, 6. main shaft, 7. roller, 8. shaft tile, 9. piston, and 10. cylinder block assembly

Since the roller continuously interacts with the cam ring during operation, shock and vibration are likely to occur under high oil pressure and high speed. Over time, it can cause damage to the cam ring, thereby affecting the overall service life of the motor. To solve this problem, this study aims to reduce the output torque pulsation, speed pulsation, shock, and vibration. The feasibility and effectiveness of the proposed design method is validated by bench testing.

2.1 Force Characterization of Cam Ring-Roller Component

2.1.1 Reaction Force Solving

To calculate the overall torque pulsation, speed pulsation, and the service life of the cam ring guide for the motor, it is necessary to determine the maximum contact stress experienced by the roller during motion. This stress is related to several factors, including radius of curvature of the cam ring, friction, hydraulic pressure, and reaction forces. Therefore, a detailed force analysis of the cam ring-piston assembly is required. The schematic of the component force is shown in Fig. 2.

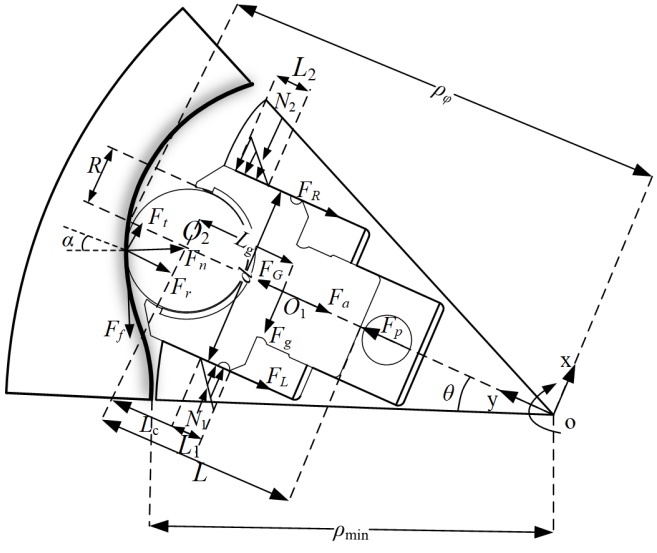

Fig. 2. Schematic of the force analysis of piston assembly

A reaction force analysis of the piston, roller, and cam ring is conducted, as shown in Fig. 2. Taking O_2, the center of a roller, as a reference point, the force and moment balance equations can be obtained as follows:

$$M_1 + M_2 + M_3 + M_4 = 0, \tag{1}$$

$$F_t + N_1 = F_f \cos\alpha + N_2 + F_g, \tag{2}$$

$$F_p + F_G = F_a + F_L + F_R + F_r + F_f \sin\alpha. \tag{3}$$

Where M_1 torque exerted by the frictional force F_f between the cam ring rail and the roller, acting at the center O_2 of the roller, M_2 is the resultant torque at the center O_2 of the roller, equivalent to the combined sliding friction forces F_L and F_R between the piston and cylinder block assembly, also acting at the center of the roller, M_3 represents the torque acting on the center of the roller O_2 due to the forces N_1 and N_2 distributed along the contact line in a triangular pattern between the generated between the piston and the inner wall of cylinder block assembly, M_4 is the inertia force F_g generated by the Gothic acceleration a_g at the croller's center O_2. F_p is the hydraulic pressure, while F_a is the inertia force generated by the acceleration of the piston relative to the cylinder block assembly, and F_G is the

centrifugal force generated by the rotation of the piston relative to the cylinder block assembly. Assume the length of the contact line between the piston and the inner wall of the cylinder block assembly be L_c, which is expressed as follows:

$$L_c = L_1 + L_2 = L_0 - \rho_\varphi + \rho_{\min}. \tag{4}$$

Here, L_0 is the contact length when the roller is positioned at the minimum pole diameter, and $\rho_{\min}$ is the minimum pole diameter.

The magnitudes of each individual moment is:

$$M_1 = F_f R, \tag{5}$$

$$M_2 = -F_R \frac{d}{2} + F_L \frac{d}{2}, \tag{6}$$

$$M_3 = N_1\left(L - \frac{1}{3}L_1\right) - N_2\left(L - \left(\rho_\varphi - \rho_{\min}\right) - L_1 + \frac{1}{3}\left(L_c - L_1\right)\right), \tag{7}$$

$$M_4 = -F_g L_g. \tag{8}$$

Here F_f iS the friction force exerted on the roller by the cam ring, R is the radius of the roller, and d is the diameter of the bottom of the piston. By substituting Eqs. (5) to (8) into Eq (1), the parameter L_1 can be determined. Due to the motor lubrication at the roller and cam ring rail contact, the resulting friction is minimal. Furthermore, based on existing literature and industry experience, friction torque is much smaller than the main transmission torque and therefore has a negligible impact. Experimental results also revealed no abnormal speed fluctuations or unstable motor operation caused by roller friction. Therefore, M_1 can be ignored. Similarly, since the distance from the roller center to the center of mass L_g is small compared to the polar diameter, and the speed pulsation of the motor under normal operating conditions is also small, the inertia force F_g generated by the corresponding acceleration a_g is negligible. Thus, M_4 can also be ignored. The equations can then be solved as follows:

$$L_1 = \frac{6\left(\rho_\varphi - \rho_{\min} - L\right)L_c - 4L_c^{\,2} + 3fdL_c}{12\left(\rho_\varphi - \rho_{\min} - L\right) + 6fd - 6L_c}. \tag{9}$$

Substitute Eq. (4) into Eq. (3) to obtain N_1 and N_2:

$$N_1 = \left(F_f \cos\alpha - F_N \sin\alpha + F_g\right)\frac{L_1^{\,2}}{2L_cL_1 - L_c}, \tag{10}$$

$$N_2 = \left(F_f \cos\alpha - F_N \sin\alpha + F_g\right)\frac{\left(L_c - L_1\right)^2}{2L_cL_1 - L_c}. \tag{11}$$

Substitute Eqs. (10) and (11) into Eq. (2) yields:

$$F_N = \frac{\Phi\left(F_G + F_p - F_a\right) - F_g}{f_2\cos\alpha - \sin\alpha + \Phi\cos\alpha + \Phi f_2\cos\alpha\sin\alpha}, \tag{12}$$

$$\Phi = \frac{2L_cL_1 - L_c}{f_1L_1^{\,2} + \left(L_c - L_1\right)^2}. \tag{13}$$

The mechanical analysis conducted by this research study is based on quasi-static processes, taking into account inertial forces, centrifugal forces, and reaction forces during motion. This approach is suitable for analyzing force variation trends under stable operating conditions but is not applicable to transient limit states occurring at high-speeds or under unstable conditions.

To ensure the physical validity and applicability of the force balance equations and moment balance equations established in this study, the derived formulas are based on the following assumptions:

1. Rotational speed range: in the analysis applies to low- to medium-speed operation of radial piston hydraulic motors (typically below 350 rpm). Within this speed range, inertial forces generated by motor components are relatively small, and the imbalance effect that occur at high speeds can be ignored.
2. Pressure range: The working pressure of the hydraulic system is assumed not to exceed the rated pressure value of 35 MPa. Pressure beyond this limit would cause significant elastic deformation of key components such as the cylinder block assembly and the piston assembly.
3. Friction conditions: It is assumed that sufficient lubrication exists between the rollers and the cam ring, as well as between piston and cylinder block assembly. Under these conditions, frictional forces are minimal, allowing the friction torque M1 and inertial torque M4 to be ignored.

Under the above operating conditions, the mechanical model derived in this paper provides a reasonable approximation of the actual operating conditions of the motor.

2.1.2 Contact Stress Analysis

In a radial piston motor, the roller acts as a rolling element that moves along the cam ring curve. As shown in Fig. 3, when the roller comes into contact with the cam ring surface, the contact area experiences localized elastic deformation due to the applied pressure.

In the contact between the roller and the cam ring, the radius of curvature of the cam ring is much larger than the radius of curvature of the roller. Therefore, it can be regarded as a problem of contact between a cylinder and a plane. The contact between the roller and the cam ring guide is thus treated as a line contact. According to the Hertzian contact theory, the maximum contact stress σmax at the center of the contact surface is expressed as follows:

$$\sigma_{\max} = \frac{2F_N}{\pi lb}, \tag{14}$$

$$b = \sqrt{\frac{4F_NR^*}{\pi lE^*}}, \tag{15}$$

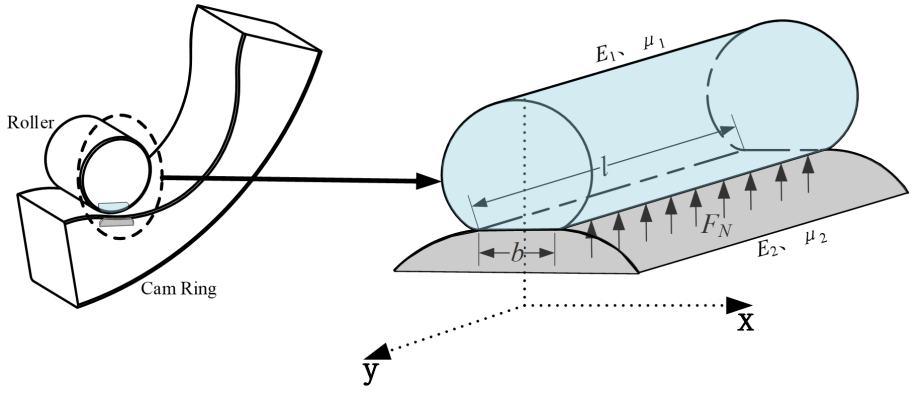

Fig. 3. Simplified model of Hertzian contact of cam ring with roller

$$\frac{1}{E^*}=\frac{\left(1-\mu_1^2\right)}{E_1}+\frac{\left(1-\mu_2^2\right)}{E_2}, \tag{16}$$

where l is the length of the contact line between the two elastic solids, which in this case equals the width of the cylindrical roller, and b is the width of the contact zone. Parameters μ_1 and μ_2, and E_1 and E_2 are the Poisson's ratios and modulus of elasticity of the two contacting elastic solids, respectively. For a hydraulic motor with a cylindrical roller, the equivalent (integrated) curvature is given as:

$$\frac{1}{R^*}=\frac{1}{R}\pm\frac{1}{R_c}, \tag{17}$$

where R is the radius of curvature of the roller, and R_c is the radius of curvature of the cam ring rail at the point of contact between the roller and the rail curve. Substituting Eqs. (15) to (17) into Eq. (14) yields:

$$\sigma_{\max}=\sqrt{\frac{F_N E_1 E_2\left(R\pm R_c\right)}{\pi l R R_c\left[E_1\left(1-\mu_2^2\right)+E_2\left(1-\mu_1^2\right)\right]}}. \tag{18}$$

2.2 Methods for Designing Multi-Step Composite Curves

The traditional iso-acceleration curve produces rapid changes in piston acceleration during the acceleration and deceleration phases. This leads to flexible shocks, and large instantaneous torque fluctuations. which in turn increase transient contact stresses, induce significant impact loads, and decrease the service life of the cam ring. To mitigate these effects, the stepped iso-acceleration curve divides the single-stage acceleration of the traditional iso-acceleration curve design into two stages. This approach reduces instantaneous torque fluctuations during both acceleration or deceleration, helping to maintain relatively smooth piston motion. However, flexible impacts still occur at the beginning and end of each section of the stepped acceleration curve, which limits its overall effectiveness.

To eliminate the problems of flexible impacts and excessive contact stress, this study proposes a multi-step composite curve, which integrates the "stepped" and "trapezoidal" acceleration curve design concepts. The original equal-acceleration zone is divided into two acceleration segments, while a transition zone is added to the deceleration phase. The result is a composite cam ring curve that is shock-free, exhibits reduced pulsation, and generates lower contact stress .

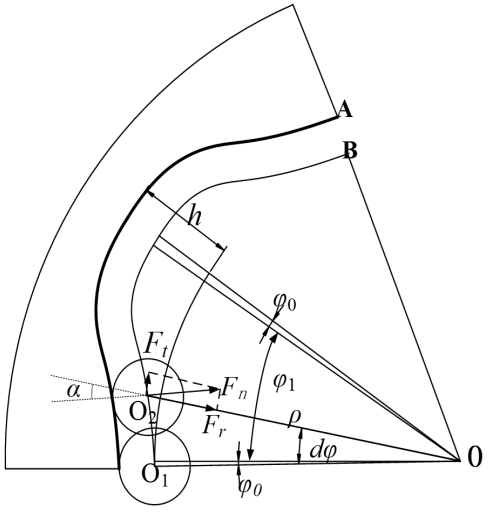

Fig. 4. Cam ring curve schema

In radial piston hydraulic motors, the cam ring guide determines the motion pattern of the piston-roller assembly. The cam ring guide curve schema is shown in Fig. 4. Curve B represents the ideal theoretical contour, i.e., the trajectory of the roller center, while curve A is the outer envelope of curve B, i.e., the actual curve of the cam ring. Depending on the theoretical design, the B curve leads to different laws of motion of the plunger assembly. In this context: the distance between the roller center O and the roller center O_2 is the pole diameter ρ, the minimum value of the pole diameter is ρ_0, the roller stroke is h, the maximum value of the pole diameter is $\rho+h$, the angle between ρ and the initial position ρ_0 is φ, the amplitude angle of the zero-speed zone is φ_0, the angle of rotation per unit time dt is $d\varphi$, α is the pressure angle, abd F_n is the reaction force of cam ring guide on the roller. The reaction force of F_n is the reaction force of the cam ring guide on the roller, which can be decomposed into tangential force F_r and radial force F_t.

The piston-roller assembly motion can be divided into the telescopic motion and the rotary motion of the piston assembly relative to the cam ring. The angular velocity v_φ and angular acceleration a_φ of the piston assembly relative to the cylinder block assembly are expressed as follows:

$$v_\varphi=\frac{d\rho}{d\varphi}, \tag{19}$$

$$a_\varphi=\frac{d^2\rho}{d\varphi^2}. \tag{20}$$

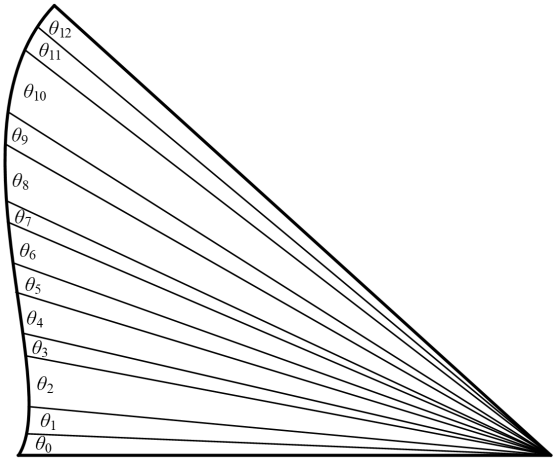

Fig. 5. Plot of amplitude distribution of multi-step composite curves

As shown in Fig. 5, the multi-step composite curve with single lift consists of 13 zones. These include: the zero-velocity zone θ_0, the first-order iso-accelerated pre-compensation zone θ_1, the first-step acceleration zone θ_2, the second-step equal-acceleration front compensation zone θ_3, the second-step acceleration zone θ_4, second-step post-compensatory zone θ_5, the uniform-velocity zone θ_6, the pre-compensation zone before the first-step iso-deceleration θ_7, the first-step iso-deceleration zone θ_8, the second-step equal-deceleration front compensation area θ_9, the second-step deceleration zone θ_{10}, the second-step post-compensation zone θ_{11}, and the zero-velocity zone θ_{12}. The displacement $\rho(j)$ at the center of the roller, angular velocity $n(j)$, and angular acceleration $a(j)$ are shown in Figs. 6 to 8.

The design process for each section is as follows: θ_0 provides a buffer for the piston when transitioning from rising to falling, avoiding impact between the roller and the cam ring guide rail due to sudden speed reversal. This zero-speed zone reduces hydraulic shock and energy loss, helps accurate oil inlet and return cycles, and improves distribution efficiency. θ_1 serves as a cushioning zone for

the piston, mitigating "flexible impact" caused by sudden changes in acceleration. The transition zone allows continuity of curvature between the zero-speed and acceleration sections. θ_2 represents the first-stage acceleration. In traditional constant-acceleration designs, excessive acceleration leads to high reaction forces and contact stress. By dividing the original single-stage acceleration into two stages (θ_2 and θ_4), acceleration in this phase is reduced, lowering reaction force and contact stress at the transition point. θ_3 connects the first- and the second-step acceleration zones, eliminating acceleration discontinuities and avoiding "flexible impact" caused by sudden acceleration changes. θ_4 denotes the second acceleration zone of the piston. Excessive acceleration in this zone can also cause excessive reaction forces and contact stresses. θ_5 provides a buffer when the piston enters the constant-speed section, reducing motor vibration caused by sudden acceleration reduction. θ_6 is the uniform-velocity zone, where piston speed remains and the acceleration is 0. θ_7~θ_{11} are symmetrical design relative to the acceleration phase. This region consists of deceleration compensation zone, deceleration zone, and transition compensation zone. θ_{12} functions identically to the zero-velocity zone θ_0, ensuring a smooth transition without impact.

The corresponding values are computed as follows:

Zero-velocity zone ($0 \le \varphi < \varphi_0$):

$$\rho = \rho_0. \tag{21}$$

First-order iso-accelerated pre-compensation zone ($\varphi_0 \le \varphi < \varphi_1$):

$$\rho_1 = \rho_0 + \frac{a_1(\varphi-\varphi_0)^3}{6\theta_1}, \tag{22}$$

First-step acceleration zone ($\varphi_1 \le \varphi < \varphi_2$):

$$\rho_2 = \rho_1(\varphi_1) + \frac{a_1\theta_1(\varphi-\varphi_1)}{2} + \frac{a_1(\varphi-\varphi_1)^2}{2}. \tag{23}$$

Second-step equal-acceleration front compensation zone ($\varphi_{1''} \le \varphi < \varphi_3$):

$$\rho_3 = \rho_2(\varphi_2) + a_1\left(\frac{1}{2}\theta_1+\theta_2\right)(\varphi-\varphi_2) + \frac{1}{2}a_1(\varphi-\varphi_2)^2 + \frac{(\mu-1)a_1(\varphi-\varphi_2)^3}{6\theta_3}. \tag{24}$$

Second-step acceleration zone ($\varphi_3 \le \varphi < \varphi_4$):

$$\rho_4 = \rho_3(\varphi_3) + a_1\left(\frac{1}{2}\theta_1+\theta_2+\theta_3+\frac{1}{2}(\mu-1)\theta_3\right)(\varphi-\varphi_3) + \frac{1}{2}\mu a_1(\varphi-\varphi_3)^2. \tag{25}$$

Second-step post-compensatory area ($\varphi_4 \le \varphi < \varphi_5$):

$$\rho_5 = \rho_4(\varphi_4) + \frac{1}{2}\mu a_1\left((\varphi-\varphi_4)^2 - \frac{(\varphi-\varphi_4)^3}{3\theta_5}\right) + a_1\left(\frac{1}{2}\theta_1+\theta_2+\theta_3+\frac{1}{2}(\mu-1)\theta_3+\mu\theta_4\right)(\varphi-\varphi_4). \tag{26}$$

Uniform velocity zone ($\varphi_5 \le \varphi < \varphi_6$):

$$\rho_6 = \rho_5(\varphi_5) + a_1\left(\frac{1}{2}\theta_1+\theta_2+\theta_3+\frac{1}{2}(\mu-1)\theta_3+\mu\theta_4+\frac{1}{2}\mu\theta_5\right)(\varphi-\varphi_5). \tag{27}$$

Compensation zone before the first-step iso-deceleration ($\varphi_6 \le \varphi < \varphi_7$):

$$\rho_7 = \rho_6(\varphi_6) - \frac{a_1(\varphi-\varphi_6)^3}{6\theta_7} + a_1\left(\frac{1}{2}\theta_1+\theta_2+\theta_3+\frac{1}{2}(\mu-1)\theta_3+\mu\theta_4+\frac{1}{2}\mu\theta_5\right)(\varphi-\varphi_6). \tag{28}$$

First-step iso-deceleration zone ($\varphi_7 \le \varphi < \varphi_8$):

$$\rho_8 = \rho_7(\varphi_7) - \frac{1}{2}a_1(\varphi-\varphi_7)^2 + a_1\left(\theta_2+\theta_3+\frac{1}{2}(\mu-1)\theta_3+\mu\theta_4+\frac{1}{2}\mu\theta_5\right)(\varphi-\varphi_7). \tag{29}$$

Second-step equal-deceleration front compensation zone ($\varphi_8 \le \varphi < \varphi_9$)

$$\rho_9 = \rho_8(\varphi_8) + a_1\left(\theta_3+\frac{1}{2}(\mu-1)\theta_3+\mu\theta_4+\frac{1}{2}\mu\theta_5\right)(\varphi-\varphi_8) - \frac{1}{2}a_1(\varphi-\varphi_8)^2 - \frac{(\mu-1)a_1(\varphi-\varphi_8)^3}{6\theta_9}. \tag{30}$$

Second-step deceleration zone ($\varphi_9 \le \varphi < \varphi_{10}$):

$$\rho_{10} = \rho_9(\varphi_9) + \frac{1}{2}\mu a_1\left((2\theta_4+\theta_5)(\varphi-\varphi_9) - (\varphi-\varphi_9)^2\right). \tag{31}$$

Second-step post-compensation zone ($\varphi_{10} \le \varphi < \varphi_{11}$):

$$\rho_{11} = \rho_{10}(\varphi_{10}) + \frac{1}{2}\mu a_1\left(\theta_5(\varphi-\varphi_{10}) - (\varphi-\varphi_{10})^2 + \frac{(\varphi-\varphi_{10})^3}{3\theta_{11}}\right). \tag{32}$$

Zero-velocity zone ($\varphi_{1''} \le \varphi < \varphi_{12}$):

$$\rho_{12} = \rho_0 + h, \tag{33}$$

where a_1 is the first-step iso-acceleration zone , and μ is the ratio of the second-step acceleration to the first-step acceleration.

$$\theta_1 = \varphi_1 - \varphi_0,\quad \theta_2 = \varphi_2 - \varphi_1,\quad \theta_3 = \varphi_3 - \varphi_2,\quad \theta_4 = \varphi_4 - \varphi_3,$$
$$\theta_5 = \varphi_5 - \varphi_4,\quad \theta_6 = \varphi_6 - \varphi_5,\quad \theta_7 = \varphi_7 - \varphi_6,\quad \theta_8 = \varphi_8 - \varphi_7,$$
$$\theta_9 = \varphi_9 - \varphi_8,\ \theta_{10} = \varphi_{10} - \varphi_9,\ \theta_{11} = \varphi_{11} - \varphi_{10},\ \theta_{12} = \varphi_{12} - \varphi_{11},$$
$$a_1 = \frac{h}{\frac{1}{2}\rho_x\left(\frac{1}{2}\theta_1+\theta_2+\frac{1}{2}(\mu+1)\theta_3+\mu\theta_4+\frac{1}{2}\mu\theta_5\right)}.$$

2.3 Optimized Design Based on SOA Algorithms

Intelligent optimization algorithms based on SOA algorithms demonstrate significant advantages in addressing complex engineering problems. Classical methods, such as genetic alorithm (GA) and particle swarm optimisation (PSO) are commonly used for parameter optimization. However, these algorithms still face limitations in tackling high-dimensional and nonlinear challenges. GA requires predefined parameters such as crossover rate and variance rate, which are highly experience-dependent and greatly influence the quality of the solution. This reliance often results in premature convergence or computational inefficiency, as its local development capability is inadequate, leading later iterations to become trapped in local optimal solutions [20-21]. In addition, PSO is prone to converge prematurely in complex scenarios due to a loss of population diversity, particularly in multi-peak function optimization. Its parameters, including inertia weights and learning factors, are highly sensitive and must be dynamically adjusted; improper configurations significantly diminish robustness [22-23]. SOA, by contrast, is a relatively new heuristic swarm intelligence algorithm inspired by the foraging and migratory flight patterns of seagulls [24-26]. This algorithm optimizes complex nonlinear problems by simulating the seagull flocking behavior , making it particularly well-suited for continuous optimization and multi-peak scenarios. Unlike PSO, which requires manual adjustment of inertia weights, SOA demonstrates greater adaptability. By incorporating spiral flight and random perturbation strategies, it maintains population diversity even in later iterations, thereby effectively addressing the limitations of PSO and GA in multi-peak problems.

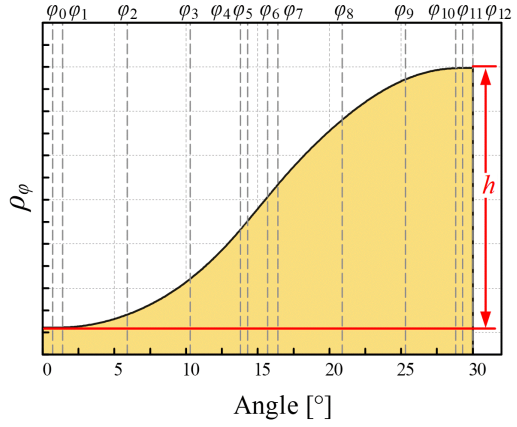

Fig. 6. Roller center displacement

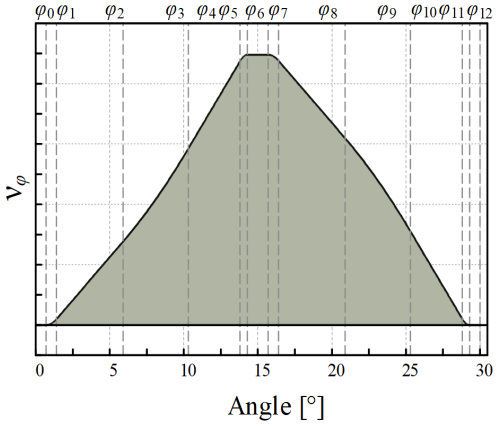

Fig. 7. Roller center angle velocity

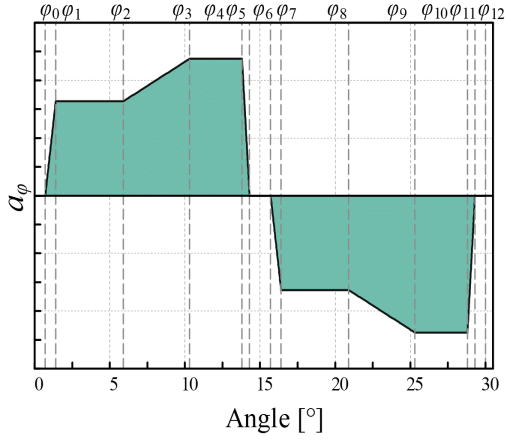

Fig. 8. Roller center angular acceleration

SOA is inspired by two characteristic behaviors of seagulls−foraging and migration− which jointly enable local exploitation near promising solutions and global exploration of the search space:

1. **Foraging behavior** (local search): During foraging, seagulls hover, circle and gradually approach the target before diving to capture the prey. This behavior reflects intensification around the current best solution. The position of the i^{th} seagull is updated as:

$$X_i(t+1) = X_i(t)e^{-\beta t} + R\left(X_{best} - X_i(t)\right), \tag{34}$$

where $X_i(t+1)$ is the position of the i^{th} seagull at iteration $t+1$, β is a parameter controlling the speed of convergence, R is a random value, which can be used to increase the randomness, and X_{best} is the current best position in the population.

2. **Migratory behavior** (global search): During migrations, seagulls travel long distances and stop at target migration points, which corresponds to diversification over a broader region to escape local optima. A simple migration-inspired update that introduces a directional (spiral/circling) drift is:

$$X_i(t+1) = X_{best} + \alpha \sin\theta\left(X_i(t) - X_{best}\right), \tag{35}$$

where α is a scaling factor to control the scope of the local search, and θ is a random angle to simulate the flight path of a circling seagull.

2.4 Contact Stress Suppression Strategy Based on SOA Algorithm

The trajectory and velocity of the piston assembly significantly affect the distribution of contact stress. As acceleration increases, the resulting inertia force is transmitted to the cam ring guide via the piston roller, leading to higher contact stresses. This effect is particularly pronounced during curve transitions, where abrupt acceleration changes can lead to sharp stress spikes, leading to increased friction and wear. Such conditions may also lead to localized material yielding or surface damage. By contrast, an optimized design of the cam ring can effectively extend the motor's service life.

In designing the inner curve of the cam ring, a zero-speed zone θ_0 is typically established both at the beginning and the end of the curve to mitigate the mechanical shock caused by sudden speed changes in the piston assembly during transitions and to reduce the leakage effect resulting from misalignment of the mating phase. Improperly setting the zero-speed zone shortens the effective working stroke of the piston and decreases the motor's output displacement, consequently reducing its output power and overall efficiency. θ_1 and θ_3 provide cushioning for the piston, improving the continuity and stability of the curve. If θ_1 and θ_3 are too small, acceleration discontinuities occur, which can easily lead to "flexible impact". Conversely, if they are too large, they compress effective acceleration interval, reducing the acceleration angle and increasing contact stress and reaction forces, which reduces the motor operating efficiency. θ_2 controls both the timing and magnitude of acceleration. A too small θ_2 yields excessive acceleration, causing peak contact stresses and accelerating rail wear, while an overly large θ_2 prolongs the acceleration cycle, affecting the output response delay. Segmented acceleration control allows smoother acceleration transitions, greatly reducing stress concentrations. The ratio of the acceleration in the second-stage to that in the first is determined by μ. If μ is too large, it causes excessive differences in acceleration, resulting in sudden velocity jumps. If μ is too small, it reduces the optimization effect.

To address the issues of local material yielding, surface damage, and reduced cam ring life caused by excessive contact stress, the SOA algorithm has been selected to optimize the design of multi-step composite curves. The fitness function is defined as the minimum value of the maximum contact stress within the deformation. Additionally, since the acceleration and deceleration zones of the cam ring curve are symmetrical, the zero-speed zone amplitude angle θ_0 is optimized alongside the three acceleration zone amplitude angles θ_1, θ_2, θ_3, as well as the ratio of the amplitude angles of the two equal-acceleration zones, μ.

$$\text{Minimize}: F(X) = \sqrt{\frac{F_N E_1 E_2 \left(R \pm R_c\right)}{\pi l R R_c \left[E_1\left(1-\mu_2^{\,2}\right) + E_2\left(1-\mu_1^{\,2}\right)\right]}},$$
$$X = [x_1, x_2, x_3, x_4, x_5] = [\theta_0, \theta_1, \theta_2, \theta_3, \mu], \tag{36}$$

Subject to: $0.5 \le \theta_0 \le 1.5$, $0.6 \le \theta_1 \le 1$, $1.2 \le \theta_2 \le 9.6$, $0.6 \le \theta_3 \le 1$, $1.3 \le \mu \le 1.7$.

Where $F(X)$ represents the maximum value of contact stress generated in the roller throughout the motion process in contact with the guide curve, θ_0 is the magnitude of the zero-speed zone, θ_1, θ_2, and θ_3 are the angular magnitudes of the three acceleration intervals. The size of the $\mu=\theta_4/\theta_2$ is defined as the ratio of the angular width of the first constant-acceleration section to that of the second constant-acceleration section.

Based on the SOA algorithm construction and optimization method, the overall process of cam ring curve optimization for a radial piston hydraulic motor is shown in Fig. 9. The main steps include:

Step 1: Start the algorithm, and define necessary parameters, including population size, iteration limits and others.

Step 2: Initialize the population (the "seagulls") and generate a random candidate solution within the defined boundaries.

Step 3: For each candidate solution in the population, calculate its corresponding maximum value of contact stress using the fitness function, and assign this as the fitness value.

Step 4: Update the positions of each sub-population using the SOA motion rules, simulating foraging and migratory behavior of seagulls to perform global and local search.

Step 5: Apply all constraints, such as boundary conditions, linear constraints, to ensure that the solution remains feasible.

Step 6: Compare the solutions in the current population to identify a new global optimal solution and record the improvement compared to the previous optimal solution.

Step 7: If the maximum number of iterations is reached, or the improvement in the solution is below a specific tolerance, continue to the next step; otherwise, return to the position update step.

Step 8: Once the stopping condition is satisfied, output the current optimal solution.

Step 9: Finish the optimization process and terminate the algorithm.

To evaluate the impact of key control parameters on the optimization results of the SOA algorithm, a sensitivity analysis was performed, namely examined the effect of factors, such as population size and maximum iteration count, comparing the optimization results and convergence behavior under different parameter configurations. The results are shown in Table 1.

Table 1. Algorithm settings and optimized results

Population size	Number of iterations	Optimal contact stress value [MPa]	Number of iterations	Dimension	Adaptive parameters
50	200	2414.9	125	5	2
100	200	2414.3	94	5	2
150	200	2414.6	98	5	2
200	200	2414.8	95	5	2

As shown in Table 1, when the population size increases from 50 to 100, the convergence speed of the algorithm improves significantly, while also the optimal fitness value decreases. When the population

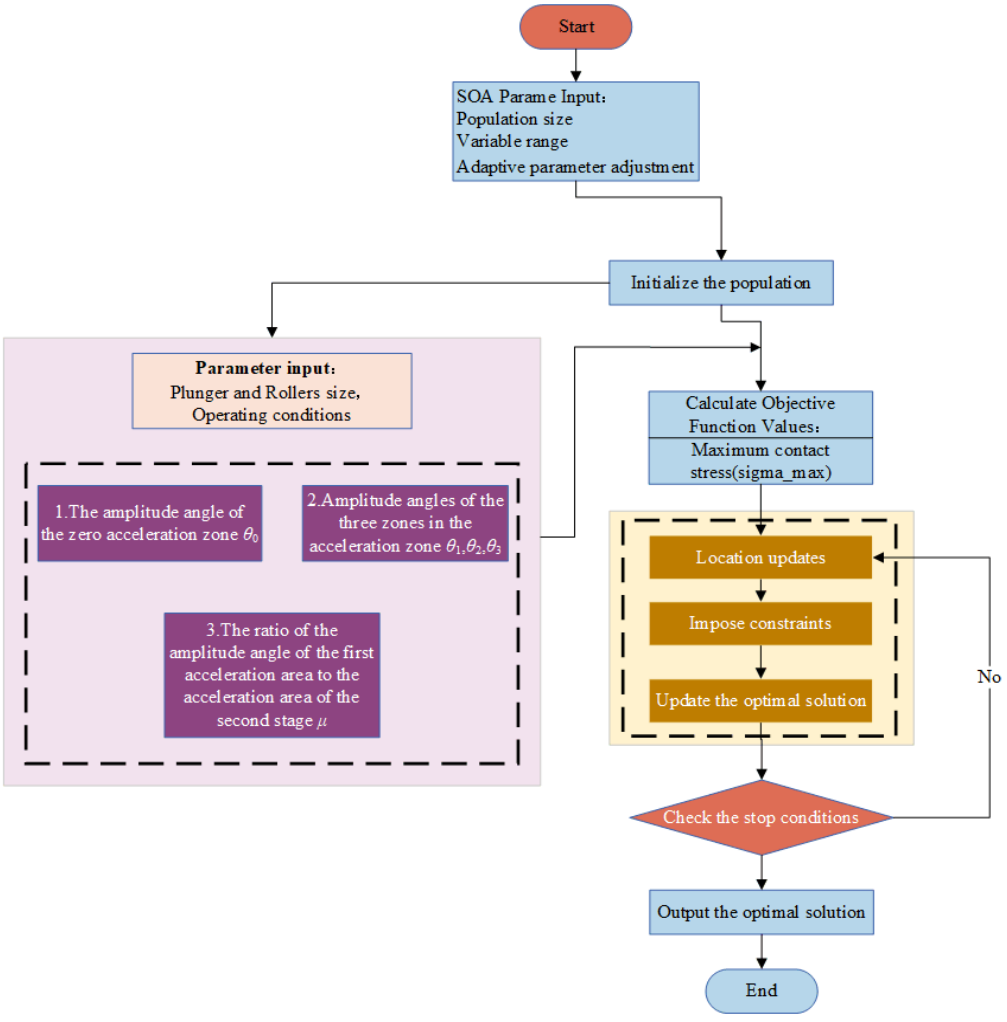

Fig. 9. Flowchart of SOA algorithm

size is further increased beyond 100, both the optimization result and the required number of iterations remain essentially stable. Therefore, a population size of 100 can be selected as the optimal balance point.

3 RESULTS AND DISCUSSION

3.1 Analysis of Optimization Results and Experimental Validation

At the end of the optimization run, the optimal solution set with the maximum value of the optimized contact stress is obtained. θ_1 and θ_3 are taken as 0.65 and 1.12, respectively, while the minimum contact stress occurs when θ_0 is 0.72, θ_2 is 7.82, and μ is 1.46. The specific iteration results are shown in Fig. 10. The algorithm converges the fastest when the number of population size is 100, and reaches convergence at the 94th iteration. Under these conditions the optimal solution yield a minimum contact stress of 2414.3 MPa.

To further validate the optimization capabilities of SOA, this study compared it against the GA and PSO algorithms under identical conditions, such as population size, fitness function, and constraints. Key performance indicators of the three algorithms, such as the best fitness value, optimization time, and average number of iterations, were recorded. The comparison results are shown in Table 2.

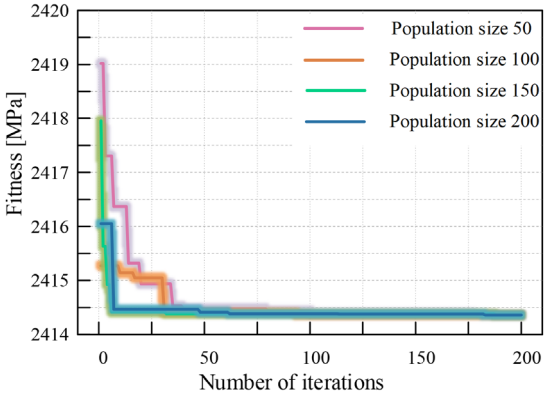

Fig. 10. Algorithm iteration results

Table 2. Comparison of the optimization performance using different algorithms

Algorithm	Optimal contact stress value [MPa]	Average convergence time [s]	Average number of iterations
GA	2456.1	10.36	105
PSO	2434.5	11.87	98
SOA	2414.3	8.89	94

As shown in Table 2, SOA achieves the lowest contact stress, outperforming PSO and GA, by 0.8 % and 1.7 % respectively. Furthermore, SOA converges faster than both GA and PSO, demonstrating higher computing efficiency. These results confirm that SOA provides superior adaptability and for complex multi-peak optimization problem.

The variation in angular acceleration of the cam ring guide curve greatly influences the motor's output characteristics, such as torque, speed, and noise. It also directly affects the contact stress between the roller and cam ring guide, which largely determines the overall service life of the motor. The maximum value of the angular acceleration of the traditional iso-acceleration curve is smaller than that of the curve designed in this study. However, the lack of transition between the zero-speed zone and the acceleration zone results in significant flexural impact during operation, which is prone to cause severe wear and tear of the guide rail at the beginning of the acceleration zone. The trapezoidal acceleration curve avoids this issue by introducing the transition zones before and after the acceleration and deceleration zones. Nevertheless, the transition zone comes at the expense of increased maximum acceleration compared to iso-acceleration curve.

In this study, amplitude optimization is carried out using the SOA. To validate the effectiveness and reasonableness of the proposed design method, the results were compared with those obtained from the the iso-acceleration curves and trapezoidal iso-acceleration curves. The angular acceleration characteristics of each curve are shown in Fig. 11 and Table 3.

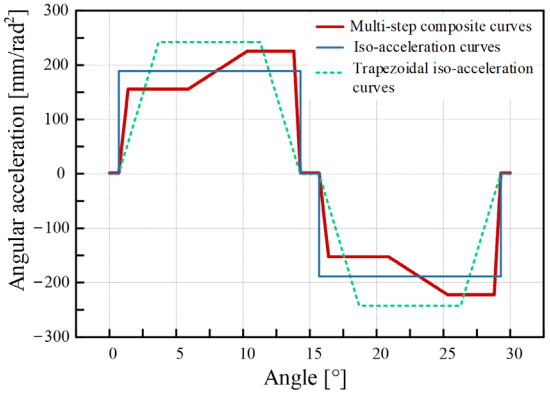

Fig. 11. Degree acceleration of each curve

Table 3 Maximum values of degree acceleration for each curve

Curve	Iso-acceleration curves	Trapezoidal iso-acceleration curves	Multi-step composite curves
Angular acceleration maxima [mm/rad²]	188.7	242.1	237.4

As shown in Fig. 12 and Table 4, curve's contact stress characteristics of each curve differ due to the different geometrical design, velocity, and acceleration distribution, radius of curvature, contact area, and stress distribution of different curves. At the beginning of the acceleration zone, the motion of the piston-roller assembly rapidly changes from low speed to high speed. During this process, angular acceleration increases sharply in a short period, causing a rapid increase of inertial forces. These forces are transmitted to the cam ring guide through the roller, resulting in a sudden stress peak in the contact area. The maximum contact stress of the iso-acceleration curve is 2557.2 MPa, while, the peak of the trapezoidal acceleration curve is 2959.7 MPa. In contrast, the maximum contact stress of the multi-step composite curve designed in this study achieves a significantly lower peak of 2414.3 MPa. This represents a reduction of 545.7 MPa compared to the peak of the maximum contact stress of the trapezoidal acceleration curve by, and 142.9 MPa compared to the peak of the iso-acceleration curve.

The reaction force of the cam ring guide to the roller directly affects both the stress distribution and the size of the contact area. Excessive reaction force can cause uneven distribution of contact stress, stress concentration, and excessive force in critical areas, thereby increasing the risk of fatigue damage. Moreover, the reaction force affects the friction at multiple interfaces; between the cam ring guide and the roller, between the roller and the piston, and between the piston and the cylinder block assembly. The increased friction leads to more wear, especially under poor lubrication conditions, ultimately shortening the service life of the parts. When the reaction force is irregular or experiences sudden changes during operation, the piston assembly or roller of the hydraulic motor may exhibit an

unstable motion trajectory. The uneven rail reaction force can trigger intermittent impacts between the roller and the rail, resulting in increased noise. Therefore, the reaction force is a critical evaluation index for assessing the smoothness and rationality of the hydraulic motor.

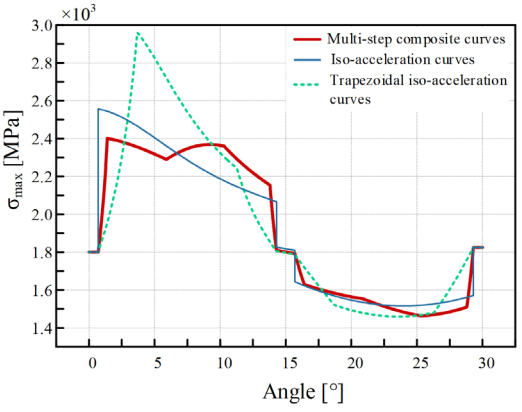

Fig. 12. Contact stresses for different curves

Table 4. Maximum contact stresses for each curve

Curve	Iso-acceleration curves	Trapezoidal iso-acceleration curves	Multi-step composite curves
Maximum contact stress [MPa]	2557.2	2959.7	2414.3

The reaction force of different curves in the oil-feeding stage is shown on Fig. 13. It can be seen that the reaction force of the iso-acceleration curve occurs at four reaction force mutation points at (the four circles in the picture), where the sudden peak jumps are represented in difference of 126.9 N, 130.2 N, 127.7 N, and 126.8 N. The mutation of the reaction force is mainly caused by the angular acceleration mutation. As indicated in Eq. (18), the sudden changes in angular acceleration will cause the mutation of R, which makes the sudden change of the maximum contact stress. In contrast, the multi-step composite curve designed in this study eliminates reaction force mutation point entirely. Its reaction force in the oil feeding stage remains lower and smoother compared to both iso-acceleration curve and trapezoidal curve.

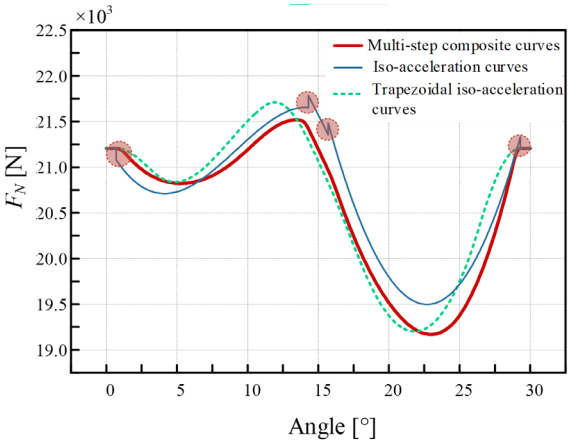

Fig. 13. Reaction force for different curves

To verify the effectiveness of the optimized multi-step composite curve design proposed in this study, the optimized multi-step

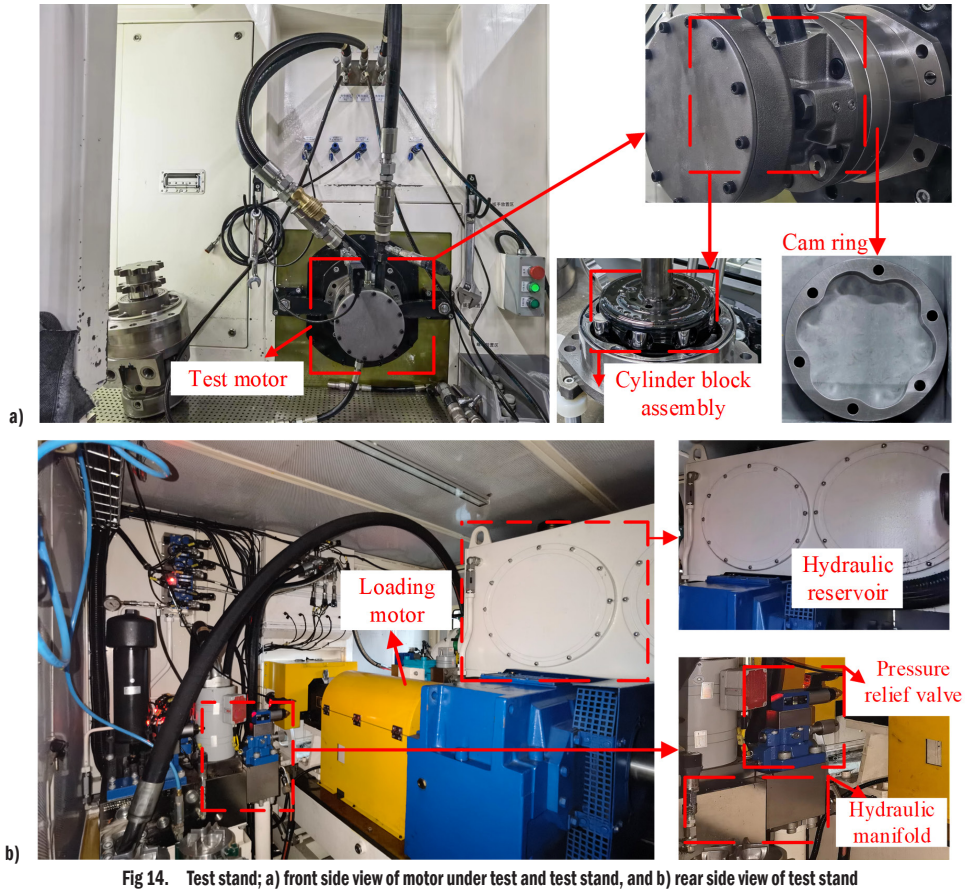

Fig 14. Test stand; a) front side view of motor under test and test stand, and b) rear side view of test stand

composite curve cam ring and iso-acceleration cam ring were manufactured and installed on a hydraulic motor test bench to test the motor speed, as shown in Fig. 14. The experimental validation analysis by the test bench shows that the cam ring processed with multi-step composite curve has improved the wear and impact problems compared with the equal acceleration curve cam ring, which can further meet the engineering requirements.

3.2 Bench Test Validation

To validate the effectiveness of the new proposed curve optimization design proposed in this study, a radial piston motor test bed is used for conducting the experiments. The radial piston hydraulic motor test bench mainly comprises the flow sensor, torque sensor, speed sensor, integrated valve manifold, oil tank, and drive motor. The industrial control computer sets the operating parameters, while the drive motor provides the initial incentive to drive the motor under stable test rotation. During the experiment, data from the tested motor is collected in real time through various sensors. Since hydraulic oil temperature significantly influences the experimental results, the system was pre-run until the hydraulic oil stabilized at 50 °C before measurements were taken. The optimized multi-step composite curve cam ring and iso-acceleration cam ring were fabricated, and the both were applied to the hydraulic motor test bench to test the motor speed condition. The main structural parameters of the radial piston motor are shown in Table 5, while the photographs of the motor under test and the test bench are shown in Fig. 14.

Table 5. Main structural parameters of radial piston hydraulic motors

Itinerary [mm]	Piston diameter [mm]	Roller diameter [mm]	Max pressure [MPa]	Effective length of piston[mm]	Min pole diameter [mm]
11.73	30	20	35	22.18	112.44

The motor speed pulsation can be expressed as:

$$\delta = \frac{n_{\max} - n_{\min}}{n_{avg}} \times 100, \tag{37}$$

where δ is speed pulsation expressed as a percentage, $n_{\max}$ is the maximum value of instantaneous speed, $n_{\min}$ is the minimum value of instantaneous speed, and n_{avg} is the average speed.

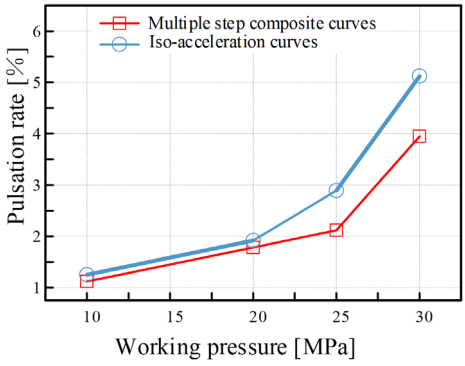

Fig. 15. Pulsation rate at experimental working pressure

The speed pulsation rates of the equal-acceleration cam ring curve and multi-step composite curve were obtained based on Eq. (37), and the relative pulsation reduction rates of the two curves were also calculated, as shown in Figs. 15 and 16. The speed pulsation of the multi-step composite curve is significantly lower than that of the equal-acceleration curve, and the relative pulsation reduction rate increases with operating pressure. At the working pressure of of 20 MPa, the pulsation reduction rate is 10.81 %, while at 30 MPa, it reaches 25.73 %. The calculation results show that the design method of the multi-step composite curve can significantly reduce the pulsation of the radial piston motor.

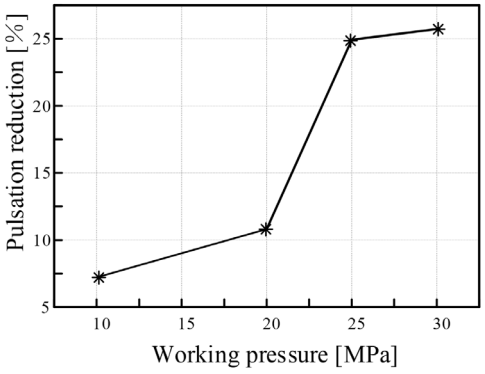

Fig. 16. Reduction of pulsation at different working pressures

4 CONCLUSIONS

In this study, we addressed the issues of high contact stress, shock vibration, and output pulsation in the design of radial piston hydraulic motor cam ring curves by constructing a constrained optimization model aimed at minimizing contact stress. By combining the global search and local refinement capabilities of SOA, we obtained optimal parameters for the amplitude angle ratio μ in the acceleration zone, the amplitude angle θ_0 in the zero-speed zone, and the amplitude angles θ_1, θ_2, and θ_3 in the acceleration zone. The optimized multi-step composite curve yields a maximum contact stress of 2414.3 MPa, representing reductions of 5.4 % and 18.3 % compared to the traditional equal-acceleration and trapezoidal curves at a speed of 100 rpm, respectively. This indicates a significant advantage in reducing wear and prolonging the cam ring service life. Bench tests further showed that the speed pulsation rate of the multi-step composite curve under 20 MPa and 30 MPa working conditions is reduced by 10.81 % and 25.73 %, respectively. Furthermore, the elimination of abrupt reaction force changes, confirms that optimized design positively impacts the smoothness of the hydraulic motor operation and energy conversion efficiency.

The cam ring curve optimization for radial hydraulic motors based on the seagull optimization algorithm (SOA) proposed in this study demonstrates both versatility and scalability, and can be applied to radial piston hydraulic motors with varying structural parameters. Optimization results show stable performance under different pressure conditions, highlighting its robustness. Looking ahead, this method holds strong potential for broader application in the design of diverse types of internal curve motors.

Nomenclature

O_2 center of the roller, [-]
O_1 center of the piston, [-]
F_p hydraulic pressure, [N]
F_a inertia force generated by the acceleration of the piston relative to the cylinder block assembly, [N]
F_G centrifugal force generated by the rotation of the piston relative to the cylinder block assembly, [N]
F_g generated by the gothic acceleration a_g on the center of the roller, [N]
F_R friction between the piston and the cavity, [N]
F_L friction between the piston and the cavity, [N]
F_f friction of the roller by the cam ring, [N]

L_0 contact length when the roller is at the minimum pole diameter, [N]
M_1 friction force F_f of the cam ring rail in contact with the roller on the center of the roller, [N·m]
M_2 sliding friction F_L and F_R between the piston and cylinder block assembly on the center of the roller, [N·m]
M_3 triangular distribution of force N_1 and N_2 along the contact line generated between the piston and cylinder block assembly wall on the center of the roller, [N·m]
M_4 inertia force F_g generated by the Gothic acceleration a_g on the center of the roller, [N·m]
N_1 the piston is subjected to positive pressure from the cylinder block assembly, [N]
N_2 the piston is subjected to positive pressure from the cylinder block assembly, [N]
L_1 triangular normal force N_2 acting on the piston length, [mm]
L_2 triangular normal force N_2 acting on the piston length, [mm]
$\rho_{\min}$ minimum pole diameter, [mm]
R radius of the roller, [mm]
d diameter of the bottom of the piston, [mm]
L_g center of mass to the center of the roller distance, [mm]
ρ_φ the polar radius of the piston center at the φ position, [mm]
L_c the length of the contact line between the piston and the inner wall of the cylinder block assembly, [mm]
a_g gothic acceleration, [mm/rad^2]
α pressure angle, [-]
f_1 sliding friction coefficient between piston and cylinder block assembly, [-]
f_2 sliding friction coefficient between roller and cam ring, [-]
l length of the contact line between the two elastic solids, [mm]
b width of the contact zone, [mm]
μ_1, μ_2 Poisson's ratios, [-]
E_1, E_2 modulus of elasticity, [MPa]
R radius of curvature of the roller, [mm]
R_c radius of curvature of the rail at the contact between the roller and the rail curve, [mm]
θ angle between the piston and its initial position, [rad]

References

[1] Dasgupta, K., Mandal, S.K., Pan, S. Dynamic analysis of a low speed high torque hydrostatic drive using steady-state characteristics. *Mech Mach Theory* 52 1-17 (2012) **DOI:10.1016/j.mechmachtheory.2011.12.004**.

[2] Tao, J., Wang, H., Liao, H., Yu, S. Mechanical design and numerical simulation of digital-displacement radial piston pump for multi-megawatt wind turbine drivetrain. *Renew Energy* 143 995-1009 (2019) **DOI:10.1016/j.renene.2019.04.159**.

[3] Zhang, X., Zhang, J., Xu, B., Yang, Z., Zhao, Q., Zhang, H. The effect of slotted hole on minimum oil film thickness of piston in radial piston hydraulic motor. *ASME/BATH 2021 Symp Fluid Power Motion Control* (2021) **DOI:10.1115/FPMC2021-69937**.

[4] Sjödin, U.I., Olofsson, U.L.O. Initial sliding wear on piston rings in a radial piston hydraulic motor. *Wear* 254 1208-1215 (2003) **DOI:10.1016/S0043-1648(03)00337-5**.

[5] Wang, H., Dong, P., Zhang, X., Zhao, Q., Fang, Y., An, G., Zhang, J., Zhang, C., Xu, B. Structure optimization design approach of friction pairs for low-temperature rise wet brake in hydraulic motor. *Case Stud Therm Eng* 61 104841 (2024) **DOI:10.1016/j.csite.2024.104841**.

[6] Fang, Y., Zhang, C., Xu, C., Xu, B., Zhang, J. Combined influence mechanism of the flexible free outer ring on contact characteristic in heavy-load cam roller bearings. *Eng Fail Anal* 156 107835 (2024) **DOI:10.1016/j.engfailanal.2023.107835**.

[7] Tang, Q., Yang, Y., Luo, C., Yang, Z., Fu, C. A novel electro-hydraulic compound braking system coordinated control strategy for a four-wheel-drive pure electric vehicle driven by dual motors. *Energy* 241 122750 (2022) **DOI:10.1016/j.energy.2021.122750**.

[8] Liu, Y., Gu, L.-c., Yang, B., Wang, S.-h., Yuan, H.-b. A new evaluation method on hydraulic system using the instantaneous speed fluctuation of hydraulic motor. *J Zhejiang Univ-SCIENCE A* 232 2674-2684 (2018) **DOI:10.1177/0954406217722576**.

[9] Zhang, N., Dong, H., Zheng, F., Gad, M., Li, D., Gao, B. Investigation of the impact of rotor- stator matching modes on the pressure pulsations of the guide vane centrifugal pump. *Ann Nucl Energy* 214 111189 (2025) **DOI:10.1016/j.anucene.2025.111189**.

[10] Zhou, D., Zhang, N., Zheng, F., Gad, M., Gao, B. Experimental investigation on the effect of the rotor-stator matching mode on velocity pulsation in the centrifugal pump with a vaned diffuser. *Nucl Eng Technol* 57 103255 (2025) **DOI:10.1016/j.net.2024.10.017**.

[11] Esmail, E.L., Saoud, F.M. Creative design of planetary gear-cam mechanisms. *Results Eng* 19 101350 (2023) **DOI:10.1016/j.rineng.2023.101350**.

[12] Giljen, Z., Nedeljković, M., Cheng, Y. The influence of pump-turbine specific speed on hydraulic transient processes. *Stroj Vestn-J Mech E* 70 231-246 (2024) **DOI:10.5545/sv-jme.2023.776**.

[13] Tang, W., Nie, Y., Zhang, Z., Lin, W., Rong, Y., Shi, Y., Ding, N. Simulation analysis and experimental study on vibration reduction performance of groove-textured friction pair surfaces. *Stroj Vestn-J Mech E* 71 207-215 (2025), **DOI:10.5545/sv-jme.2024.1209**.

[14] Gao, S., Li, Y., Zhang, Y., Ji, S., Wang, J. Lifespan evaluation for a standard rv reducer based on fatigue strength theory. *Stroj Vestn-J Mech E* 70 452-565 (2024) **DOI:10.5545/sv-jme.2023.897**.

[15] Shao, Y., Chen, Y., Xiao, X., Zheng, M., He, W. Design and Stress Analysis of Bevel Line Gears with Vertical Flank Suitable for Micro Machining. *Stroj Vestn-J Mech E* 70 483-493 (2024) **DOI:10.5545/sv-jme.2024.917**.

[16] Zhang, X.L., Zhang, J.H., Zhang, H.J., Optimized design of cam ring curve of cam lobe radial-piston motor. *J Huazhong Univ Sci Technol, Nat Sci Ed* 49 30-35 (2021) **DOI:10.13245/j.hust.211005**. (in Chinese)

[17] Li, J.X., Kang, S.P., Yang, J. Internal curve optimization of radial plunger hydraulic motor with improved particle swarm optimization. *Mod Manuf Eng* 2 69-75 (2025) **DOI:10.16731/j.cnki.1671-3133.2025.02.009**. (in Chinese)

[18] Zhou, C., Hu, B., Chen, S., Ma, L. Design and analysis of high-speed cam mechanism using Fourier series. *Mech Mach Theory* 104 118-129 (2016) **DOI:10.1016/j.mechmachtheory.2016.05.009**.

[19] Zhang, C., Tan, H., Fang, Y., Zhang, X., Yang, Y., Duan, Y. et al. Deformation pre-compensated optimization design of cam ring for low pulsation hydraulic motors. *J Zhejiang Univ-SCIENCE A* 24 130-145 (2023) **DOI:10.1631/jzus.A2200552**.

[20] Topaloglu, I., Bektaş, E., Yiğit, M.E., Korkmaz, F. Design and experimental implementation of skewed stator structured pm generator using multi-objective genetic algorithm for gearless direct driven wind system. *Ain Shams Eng J* 15, 103067 (2024) **DOI:10.1016/j.asej.2024.103067**.

[21] Iñiguez-Lomeli, F.J., Garcia-Capulin, C.H., Rostro-Gonzalez, H. A hardware architecture for single and multiple ellipse detection using genetic algorithms and high-level synthesis tools. *Microproc Microsyst* 111 105106 (2024) **DOI:10.1016/j.micpro.2024.105106**.

[22] Chang, H., Yang, J., Wang, Z., Peng, G., Lin, R., Lou, Y., Shi, W., Zhou, L. Efficiency optimization of energy storage centrifugal pump by using energy balance equation and non-dominated sorting genetic algorithms-II. *J Energy Storage* 114 115817 (2025) **DOI:10.1016/j.est.2025.115817**.

[23] McNulty, A., Ombuki-Berman, B., Engelbrecht, A. A comparative study of evolutionary algorithms and particle swarm optimization approaches for constrained multi-objective optimization problems. *Swarm Evolut Comput* 91 101742 (2024) **DOI:10.1016/j.swevo.2024.101742**.

[24] Dhiman, G., Kumar, V. Seagull optimization algorithm: Theory and its applications for large-scale industrial engineering problems. *Knowl-Based Syst* 165 169-196 (2019) **DOI:10.1016/j.knosys.2018.11.024**.

[25] Altay, E.V., Altay, O., Özçevik, Y. A comparative study of metaheuristic optimization algorithms for solving real-world engineering design problems. *CMES - Comput Model Eng Sci* 139 1039-1094 (2023) **DOI:10.32604/cmes.2023.029404**.

[26] Xian, S., Chen, K., Cheng, Y. Improved seagull optimization algorithm of partition and xgboost of prediction for fuzzy time series forecasting of covid-19 daily confirmed. *Adv Eng Softw* 173 103212 (2022) **DOI:10.1016/j.advengsoft.2022.103212**.

Acknowledgements *This work is supported by the National Natural Science Foundation of China (51805228), the Natural Science Foundation of the Jiangsu Higher Education Institutions of China (22KJB460021, 23KJA460006) and Changzhou Leading Innovative Talents Introduction and Cultivation Project the (CQ20210093, CQ20220089).*

Received: 2025-05-16, revised: 2025-07-16, accepted: 2025-08-27
as Original Scientific Paper.

Data availability *The data supporting the findings of this study are included in the article.*

Author contribution *Bowen Zhang: Conceptualization, Formal Analysis, Methodology, Writing - original draft, Writing - review & editing; Shaopeng Kang: Conceptualization, Funding Acquisition, Resources, Supervision, Validation, Writing - original draft, Writing - review & editing; Runze Zhou: Data Curation, Supervision; Hongbin Qiang: Resources; Jing Yang: Visualization; Kailei Liu: Underlying Acquisition; Yunkai Zhou: Validation.*

Optimizacija krivulje odmikalnega obroča za radialni hidravlični motor na osnovi algoritma obnašanja galebov

Povzetek *S pospešenimi prilagoditvami globalne energetske strukture se intenzivnost izkoriščanja strateških mineralnih virov še naprej povečuje. Zaradi rastočega povpraševanja po gradbenih strojih in opremi se radialni batni hidravlični motorji, znani po nizkih vrtilnih hitrostih in visokih navorih, vse pogosteje uporabljajo v težkih rudarskih strojih in opremi. Zasnova krivulje odmikalnega obroča radialnega batnega hidravličnega motorja še vedno predstavlja ključne izzive, kot so visoke kontaktne napetosti, izrazite pulzacije izhodne hitrosti. Ta članek predlaga metodo večstopenjske optimizacije sestavljene krivulje, ki temelji na algoritmu optimizacije obnašanja galebov (SOA). Metoda združuje koncepte stopničaste in trapezne zasnove pospeševalne krivulje ter uporablja SOA algoritem za obvladovanje omenjenih izzivov. Algoritem SOA je prilagodljivejši od genetskega algoritma in algoritma rojev delcev, saj ohranja raznolikost populacije tudi v poznejših fazah iteracije. S tem učinkovito premaguje omejitve drugih algoritmov pri reševanju problemov z več lokalnimi optimumi. Zasnovan je bil optimizacijski model krivulje odmične obroče za zmanjšanje kontaktnih napetosti na podlagi teoretičnega modeliranja in dinamične analize. Izvedena je bila večparametročna optimizacija ključnih parametrov, kot so razmerje amplituda–kot v pospeševalni coni in amplituda–kot v coni ničelne hitrosti. Tako je bila pridobljena sestavljena krivulja odmikalnega obroča, za katero so značilne manjše napetosti, manjša pulzacija in obratovanje brez udarcev. Učinkovitost metode je bila potrjena z laboratorijskimi testi, ki so pokazali, da je največja kontaktna napetost optimizirane večstopenjske sestavljene krivulje pri hitrosti 100 vrt/min zmanjšana za 5,4 % in 18,3 % v primerjavi s tradicionalno enakomerno pospeševalno krivuljo oziroma trapezno krivuljo. Poleg tega se stopnja pulzacije hitrosti zmanjša za 10,81 % in 25,73 % pri tlaku olja 20 MPa oziroma 30 MPa, brez nenadnih sprememb reakcijske sile in z zmanjšanjem udarnih pulzacij med obratovanjem.*

Ključne besede *radialni batni hidravlični motor, optimizacija odmikalnega obroča, algoritem optimizacije obnašanja galebov, kontaktna napetost, pulzacija hitrosti*